Sublattice pairing in pyrochlore Heisenberg antiferromagnets

Cecilie Glittum [1,2] and Olav F. Syljuåsen [2]
[1]*T.C.M. Group, Cavendish Laboratory, JJ Thomson Avenue, Cambridge CB3 0HE, United Kingdom*
[2]*Department of Physics, University of Oslo, P.O. Box 1048 Blindern, N-0316 Oslo, Norway*

(Received 16 May 2023; accepted 29 June 2023; published 11 July 2023)

We argue that classical pyrochlore Heisenberg antiferromagnets with small further-neighbor couplings can order in a state where pairs of sublattices form antiparallel spirals. The spiral ordering wave vectors of the two pairs are in general different from each other and are constrained by which sublattices are being paired. This sublattice pairing state generally breaks inversion and most rotation symmetries. Its existence depends on the antiferromagnetic nearest-neighbor coupling which favors the spins on each tetrahedron to sum to zero. To substantiate our argument, we extend the nematic bond theory, a diagrammatic large-N_s method, to non-Bravais lattices, and we demonstrate that the predicted state is indeed realized at low temperatures in a large region of exchange coupling space. We also carry out a spin wave calculation which suggests that the sublattice pairing state is coplanar.

DOI: 10.1103/PhysRevB.108.014413

I. INTRODUCTION

The Heisenberg antiferromagnet on the pyrochlore lattice has gotten much attention as it is a spin liquid candidate. This is mainly motivated by the antiferromagnetic (AFM) nearest-neighbor classical model, which is predicted to be disordered at all temperatures [1–4]. However, real pyrochlore magnetic materials are seldom described by the nearest-neighbor model alone. It is, therefore, important to understand the effects of further-neighbor couplings and when and what magnetic order they may cause.

Ordering transitions as a result of adding further-neighbor couplings has been studied in mean-field theory [2], and it is known that further-neighbor interactions induce symmetry breaking in the purely classical J_1-J_2 model [5–8].

The third nearest-neighbor couplings are known to be important for several pyrochlore materials and in many cases more important than the second nearest-neighbor couplings [9–11]. There are two inequivalent third nearest-neighbor couplings on the pyrochlore lattice: J_{3a}, which goes in the direction of J_1, and J_{3b}, which goes across the hexagons (see Fig. 1). Existing theoretical works including third nearest-neighbor couplings either treat the two as equal or set J_{3b} to zero when studying ordering transitions [5,12,13].

In this article we propose another kind of ordered state for pyrochlore Heisenberg antiferromagnets: a sublattice pairing (SLP) state, where sublattices pair up, and each pair form antiparallel spirals. We treat the Heisenberg antiferromagnets classically and focus on the hierarchy of magnetic scales $J_1 > J_{3b} \gtrsim J_2, J_{3a}$. This might be important for the $Gd_2B_2O_7$ pyrochlores [9] and the AFe_2O_4 spinels [11].

The Hamiltonian is

$$H = \frac{1}{2}\sum_{\vec{r},\vec{r}'} J(\vec{r}' - \vec{r})\, \vec{S}_{\vec{r}} \cdot \vec{S}_{\vec{r}'}, \tag{1}$$

where the exchange couplings are illustrated in Fig. 1. The pyrochlore lattice has four fcc sublattices. We label the spins by their unit cell $\vec{R}$ and the sublattice index i rather than

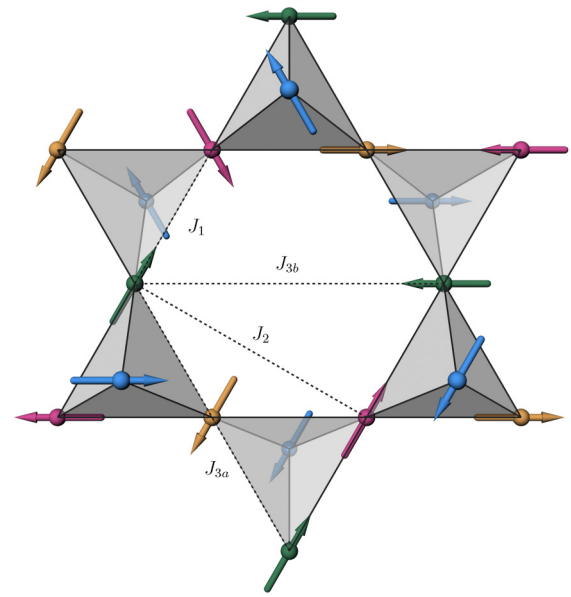

FIG. 1. Pyrochlore lattice with spins showing an example of an SLP state where sublattices 0 (pink) and 1 (blue) are antiparallel and ordered at $\vec{Q}_{(0,1)} = (0, -4\pi/3, 4\pi/3)$ and sublattices 2 (green) and 3 (yellow) are antiparallel and ordered at $\vec{Q}_{(2,3)} = (0, 4\pi/3, 4\pi/3)$. The first ($J_1$), the second ($J_2$), and the two inequivalent third (J_{3a} and J_{3b}) nearest-neighbor couplings are shown. The blue spins show how layers of triangular planes separated by kagome layers of the remaining sublattices are ordered in 120° spirals for the J_1-J_{3b} model.

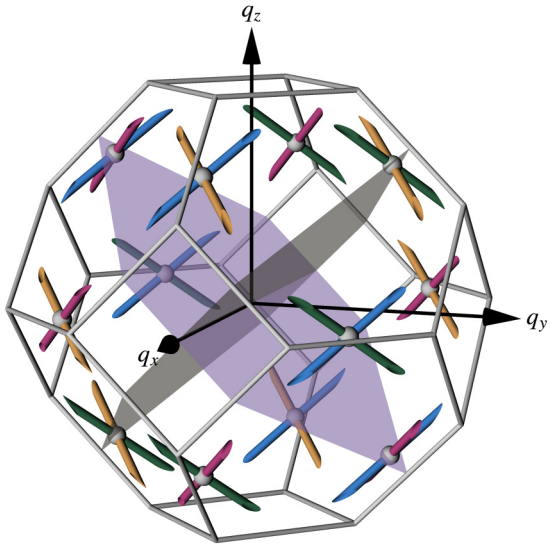

FIG. 2. The first Brillouin zone (1BZ) showing planes $\vec{Q}_{(0,1)}$ (purple) and $\vec{Q}_{(2,3)}$ (gray) satisfying Eq. (5), and J_{3b} energy minimal lines for sublattices 0 (pink), 1 (blue), 2 (green), and 3 (yellow). The lines intersect at $(0, 4\pi/3, 4\pi/3)$ and symmetry-related points (light gray). The line intersection points in the planes correspond to the possible spiral ordering wave vectors for SLP between sublattices (0,1) and (2,3).

the position $\vec{r} = \vec{R} + \vec{\alpha}_i$. $\vec{R}$ is constructed from the fcc primitive lattice vectors $\vec{a}_1 = (0, 1/2, 1/2)$, $\vec{a}_2 = (1/2, 0, 1/2)$, and $\vec{a}_3 = (1/2, 1/2, 0)$, where we have set the cubic lattice constant to unity. The sublattice vectors $\vec{\alpha}_i$ are $\vec{\alpha}_0 = (0, 0, 0)$ and $\vec{\alpha}_i = \vec{a}_i/2$ for $i = \{1, 2, 3\}$. We choose energy units $J_1 = 1$.

II. SUBLATTICE PAIRING

An AFM nearest-neighbor coupling favors the spins on each tetrahedron to sum to zero [1,2], i.e., $\sum_{i=0}^{3} S_{\vec{R},i} = 0$ for the up-tetrahedra and $\sum_{i=0}^{3} \vec{S}_{\vec{R}-\vec{a}_i,i} = 0$ for the down-tetrahedra. If each sublattice orders in a single-$\vec{q}$ spiral state $S_{\vec{R},i} = \vec{u}_i \cos \vec{Q}_i \cdot \vec{R} + \vec{v}_i \sin \vec{Q}_i \cdot \vec{R}$, the Fourier-transformed condition for the up-tetrahedra gives

$$\sum_i \left[(\vec{u}_i - i\vec{v}_i)\delta_{\vec{q},\vec{Q}_i} + (\vec{u}_i + i\vec{v}_i)\delta_{\vec{q},-\vec{Q}_i}\right] = 0, \tag{2}$$

where the δ's should be understood modulo a reciprocal lattice vector. This is satisfied by what we refer to as an SLP state. In an SLP state, the sublattices form pairs, such that each sublattice pair (i, j) shares the same ordering wave vector $\vec{Q}_{(I,j)}$ and has antiparallel spins:

$$\vec{S}_{\vec{R},i} = \vec{u}_{(i,j)} \cos(\vec{Q}_{(i,j)} \cdot \vec{R}) + \vec{v}_{(i,j)} \sin(\vec{Q}_{(i,j)} \cdot \vec{R}), \tag{3}$$

$$\vec{S}_{\vec{R},j} = -\vec{S}_{\vec{R},i}, \tag{4}$$

where $\vec{u}_{(i,j)}$ and $\vec{v}_{(i,j)}$ are orthonormal vectors. If the two ordering wave vectors are different, this state satisfies also the condition for the down-tetrahedra if

$$[\vec{Q}_{(i,j)} \cdot (\vec{a}_i - \vec{a}_j)] \mod 2\pi = 0 \tag{5}$$

for both pairs of sublattices. Figure 2 shows the planes in momentum space where $\vec{Q}_{(0,1)}$ and $\vec{Q}_{(2,3)}$ satisfy this equation.

The ordering wave vectors $\vec{Q}_{(i,j)}$ are generally found by minimizing the energy. As the SLP state minimizes the J_1 terms of the energy, it is sufficient to minimize the further-neighbor energy terms subject to the condition Eq. (5). As a first example, we consider the pure J_1-J_{3b} model. The third nearest neighbors on the pyrochlore lattice couple sites from the same fcc sublattices, and J_{3b} alone effectively reduces each of the four fcc sublattices to a set of decoupled parallel triangular planes. An AFM J_{3b} will then favor 120° order in each triangular plane. For a single plane, there are two such chiral ordering vectors, given by clockwise and counterclockwise 120° rotations. Since the triangular planes in a set are decoupled, the addition of any wave vector orthogonal to the triangular planes will still give 120° order in each plane, but with an additional interplane rotation. This gives rise to a set of lines in momentum space for each of the four sublattices, along which the J_{3b} part of the energy is minimal. This is illustrated in Fig. 2. These lines would correspond to rods of scattering if $J_1 = 0$. The lines intersect at points where the J_{3b} energy of two sublattices is minimized by the same $\vec{Q}$ vector. These wave vectors are given by $(0, 4\pi/3, 4\pi/3)$ and symmetry-related vectors and lie also on the planes satisfying the tetrahedron condition Eq. (5). The example shown in Fig. 2 is $\vec{Q}_{(0,1)} = \pm(0, 4\pi/3, -4\pi/3)$ and $\vec{Q}_{(2,3)} = \pm(0, 4\pi/3, 4\pi/3)$, and the corresponding SLP 120° configuration is illustrated in Fig. 1.

To study the ordering wave vectors for the more general J_1-J_2-J_{3a}-J_{3b} model, we make use of the fact that this model can be recast into a $\tilde{J}_1$-$\tilde{J}_{3a}$-J_{3b} model when the tetrahedra conditions are satisfied, with $\tilde{J}_1 = J_1 - J_2$ and $\tilde{J}_{3a} = J_{3a} - J_2$ [7]. $\vec{Q}_{(i,j)}$ is then found as the wave vector that satisfies Eq. (5) and minimizes the $\tilde{J}_{3a}$-J_{3b} energy sum of the pairing fcc sublattices i and j. For $-3 \leqslant \tilde{J}_{3a}/J_{3b} \leqslant 1$ with AFM J_{3b}, we find that $\vec{Q}_{(i,j)}$ is given by the vectors symmetry related to

$$\vec{Q} = \begin{cases} (0, h, h), & \tilde{J}_{3a}/J_{3b} \leqslant \sqrt{2} - 1, \\ (2\pi, h - 2\pi, h - 2\pi), & \tilde{J}_{3a}/J_{3b} > \sqrt{2} - 1, \end{cases} \tag{6}$$

with h=2 arccos$[-(1 + \tilde{J}_{3a}/J_{3b})/2]$, that satisfy Eq. (5).

When $\tilde{J}_{3a}/J_{3b} < -3$ for AFM J_{3b}, $\tilde{J}_{3a}/|J_{3b}| < 1$ for ferromagnetic (FM) J_{3b}, or $\tilde{J}_{3a} < 0$ for $J_{3b} = 0$, the minimum occurs at Γ. The associated SLP state, SLP-Γ, where both the ordering vectors are equal to Γ, covers both the collinear Néel state [7] and the coplanar Palmer-Chalker state [14]. When $\tilde{J}_{3a} > |J_{3b}|$, the minimum occurs at X_{1BZ}.

For $\tilde{J}_{3a}/J_{3b} = -1$, there is a line minimum: $\vec{Q} = (l, \pi, \pi)$ for AFM J_{3b} and $\vec{Q} = (l, 0, 0)$ for FM J_{3b}.

III. NEMATIC BOND THEORY

In order to investigate the occurrence of SLP states in the pyrochlore Heisenberg model, Eq. (1), we employ the nematic bond theory (NBT) [15]. The NBT is a large-N_s approximation, where N_s is the number of spin components, leading to a set of self-consistent equations for classical Heisenberg magnets. It has previously been employed for the square, cubic, and triangular lattices [15–18]. In this article, we extend the NBT to non-Bravais lattices with m sublattices. Consequently, quantities like the exchange coupling $J_{\vec{q}}$ and the self-energy $\Sigma_{\vec{q}}$ become $m \times m$ matrices in sublattice space.

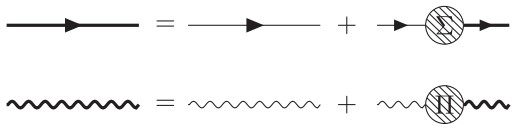

FIG. 3. Dyson equations for the renormalized spin propagator $K_{\vec{q}}^{-1}$ (bold solid line) and the renormalized constraint propagator $D_{\vec{q}}$ (bold wavy line).

In momentum space, the Hamiltonian is

$$H = \sum_{\vec{q}} \sum_{ij} J_{\vec{q},ij} \vec{S}_{-\vec{q},i} \cdot \vec{S}_{\vec{q},j}, \tag{7}$$

where the $\vec{q}$-sum goes over the first Brillouin zone, and i and j are sublattice indices. In the NBT, the classical spins are integrated out by introducing a constraint field $\lambda_{\vec{R},i}$ ensuring the unit length of the spins, $|\vec{S}_{\vec{R},i}| = 1$, through

$$\delta(|\vec{S}_{\vec{R},i}| - 1) = \int_{-\infty}^{\infty} \frac{\beta d\lambda_{\vec{R},i}}{\pi} e^{-i\beta\lambda_{\vec{R},i}(\vec{S}_{\vec{R},i}\cdot\vec{S}_{\vec{R},i}-1)}. \tag{8}$$

The remaining integrals over the constraint field are treated separately for the average constraints Δ_i and the fluctuations around the average. The average constraints are treated by the saddle-point approximation, and the fluctuations are treated through diagrammatic perturbation theory (large-N_s approximation). As in Ref. [15], the diagrams consist of solid and wavy lines, representing spin and constraint propagators, respectively. In addition to sublattice indices, we have here also included directions to the spin propagators to allow for breaking of inversion symmetry. The spin propagator $K_{\vec{q},ij}^{-1}$ is then to be understood as carrying momentum $\vec{q}$ from i to j.

The spin and constraint propagators are renormalized by the self-energy $\Sigma_{\vec{q}}$ and the polarization $\Pi_{\vec{q}}$, respectively, through the Dyson equations in Fig. 3. The large-N_s approximation is performed through a set of self-consistent equations for the self-energy and the polarization, which are shown diagramatically in Fig. 4. These equations approximate the self-energy and the polarization by infinite resummations of classes of diagrams excluding vertex corrections. Combining the Dyson equations and the self-consistent equations, the NBT equations are [15]

$$K_{\vec{q},ij} = J_{\vec{q},ij} + \Delta_i \delta_{ij} - \Sigma_{\vec{q},ij}, \tag{9}$$

$$D_{\vec{q},ij}^{-1} = \frac{N_s}{2} \sum_{\vec{p}} K_{\vec{q}+\vec{p},ij}^{-1} K_{\vec{p},ji}^{-1}, \tag{10}$$

$$\Sigma_{\vec{q},ij} = -\sum_{\vec{p}\neq 0} K_{\vec{q}-\vec{p},ij}^{-1} D_{\vec{p},ij}, \tag{11}$$

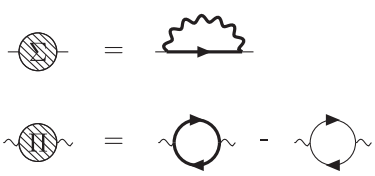

FIG. 4. Self-consistent equations for the self-energy $\Sigma_{\vec{q}}$ and the polarization $\Pi_{\vec{q}}$.

where $K_{\vec{q}}^{-1}$ is the renormalized spin propagator and $D_{\vec{q}}$ is the renormalized constraint propagator.

As the constraint field now has a sublattice index, we get a separate saddle-point equation for each sublattice,

$$\frac{N_s T}{2V} \sum_{\vec{q}} K_{\vec{q},ii}^{-1} = 1, \tag{12}$$

where $V = L^3$ is the number of unit cells. These m saddle-point equations give the temperature T. They must all give the same temperature for the solution to be physical. Following the derivation in Ref. [17], the free energy per unit cell (excluding vertex corrections) is

$$\begin{aligned} f = &-\sum_i \Delta_i + \frac{T}{2V} \sum_{\vec{q}} \ln\det\left(\frac{T^2}{2V} D_{\vec{q}}^{-1}\right) \\ &- \frac{N_s T}{2V} \sum_{\vec{q}} \left[\ln\det\left(T K_{\vec{q}}^{-1}\right) - \mathrm{Tr}\left(K_{\vec{q}}^{-1}\ \Sigma_{\vec{q}}\right)\right] \\ &- m\frac{N_s - 1}{2} T \ln \pi. \end{aligned} \tag{13}$$

The self-consistent equations are solved by iteration starting from a random self-energy and equal values of the Δ_i's. Each iteration gives an overall negative contribution to the self-energy. To avoid the general increase in temperature associated with this, the Δ_i's are renormalized in every iteration by subtracting from them the minimum eigenvalue among all $\Sigma_{\vec{q}}$. In addition, each Δ_i is adjusted very slightly so that Eq. (12) gives the same value of the temperature for all sublattices. We iterate until the temperature converges and then employ $K_{\vec{q}}^{-1}$, $\Sigma_{\vec{q}}$, and $D_{\vec{q}}$ to calculate the free energy. For each initial value of the Δ_i's, we thereby obtain f and $K_{\vec{q}}^{-1}$ with a corresponding T.

For a random initial self-energy, the NBT might not converge to the lowest temperatures. In those cases we initialize the iterations using an estimated form of $K_{\vec{q}}^{-1}$ with peaks at suitable momenta. If different initial conditions converge to different states, we pick the state with the lowest free energy.

To get information about the spin correlations we calculate the quantity

$$A_{\vec{q}} \equiv \sum_{ij} K_{\vec{q},ij}^{-1} e^{-i\vec{q}\cdot(\alpha_i - \alpha_j)}. \tag{14}$$

$A_{\vec{q}}$ is periodic with twice the reciprocal lattice vectors and the associated extended Brillouin zone (EBZ) is a truncated octahedron with dimensions twice those of the first Brillouin zone (1BZ) of the fcc lattice. $A_{\vec{q}}$ is closely related to the spin structure factor $S(\vec{q}) \equiv \sum_{ij} \langle \vec{S}_{-\vec{q},i} \cdot \vec{S}_{\vec{q},j} \rangle e^{i\vec{q}(\alpha_i - \alpha_j)} = N_s T (A_{\vec{q}} + A_{-\vec{q}})/4$. While $S(\vec{q})$ is manifestly inversion symmetric, $A_{\vec{q}}$ is not as it reflects the symmetries of the self-energy $\Sigma_{\vec{q},ij}$. We take lack of inversion symmetry in $A_{\vec{q}}$ to indicate that the spin state breaks inversion symmetry.

IV. RESULTS

For the pure AFM nearest-neighbor Hamiltonian, the NBT gives no symmetry breaking down to the lowest temperature studied ($T \simeq 10^{-9}$), and $A_{\vec{q}}$ shows O_h symmetric extended maxima on the square surfaces of the EBZ with pinch points at X_{EBZ} [19].

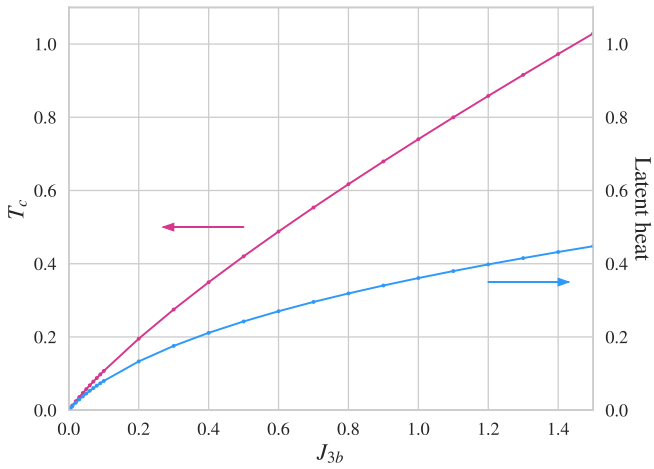

FIG. 5. Phase transition temperature T_c (pink) and latent heat (blue) vs J_{3b} for the transition into the SLP state. $J_2 = J_{3a} = 0$. $L = 36$.

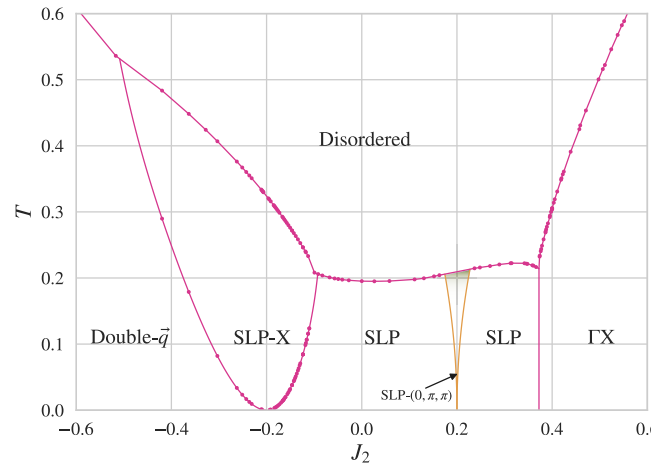

FIG. 6. T vs J_2 phase diagram for $J_{3b} = 0.2$. Various system sizes $L = 26$–60. $J_{3a} = 0$. The solid curves, based on discontinuities in the free energy (dots), are first-order phase transitions. The yellow lines around the SLP-$(0, \pi, \pi)$ phase are uncertain as the NBT does not converge in the shaded region close to the disordered phase.

For the J_1-J_{3b} model with $J_{3b} = 0.2$, the maxima of $A_{\vec{q}}$ at high temperature occurs at $\mathrm{W}_{\mathrm{EBZ}}$. As the temperature is lowered, these maxima move into the hexagonal EBZ surfaces keeping the full O_h symmetry. Then at $T_c = 0.195$ (for $L = 36$) the NBT free energy reveals a first-order phase transition into a low-temperature phase with a total of eight peaks in $A_{\vec{q}}$ in the EBZ [20]: at $\vec{Q}_{(0,1)} + \vec{b}_1 + n_2\vec{b}_2 + n_3\vec{b}_3$ for $n_2, n_3 \in \{0, 1\}$, and at $\vec{Q}_{(2,3)} + \vec{b}_2 + n_1\vec{b}_1$, $\vec{Q}_{(2,3)} + \vec{b}_3 + n_1\vec{b}_1$ for $n_1 \in \{0, 1\}$, with $\vec{Q}_{(0,1)} = (0, -4\pi/3, 4\pi/3)$ and $\vec{Q}_{(2,3)} = (0, 4\pi/3, 4\pi/3)$. $\vec{b}_i$ denote the reciprocal lattice vectors for the fcc Bravais lattice. The symmetry of $A_{\vec{q}}$ is thus reduced from O_h to C_{2v}. In particular, inversion symmetry and all three- and fourfold symmetries are broken. When adding also $A_{-\vec{q}}$ to obtain the spin structure factor, the C_{2v} symmetry is increased to D_{2h}. The peaks in $A_{\vec{q}}$ can be explained as originating from a 120° SLP state where antiparallel spirals on sublattices 0 and 1 order at $\vec{Q}_{(0,1)}$ and antiparallel spirals on sublattices 2 and 3 order at $\vec{Q}_{(2,3)}$. We find that such first-order transitions into the C_{2v} symmetric 120° SLP phase occur for all positive values of J_{3b} (see Fig. 5).

We next check the stability of the SLP phase when adding J_2. The finite-temperature phase diagram obtained using the NBT for $J_{3b} = 0.2$ is shown in Fig. 6. The SLP phase is stable in the region $-0.2 \leqslant J_2 < 0.372$, and the ordering wave vectors follow Eq. (6). For FM $J_2 < -0.2$, the SLP state becomes unstable to a double-$\vec{q}$ state, reminiscent of the multi-$\vec{q}$ states investigated in Refs. [6–8,21], where two ordering vectors are present on *all* sublattices.

For $J_2 = -0.2$, we find a special case of the SLP state, labeled SLP-X in Fig. 6, where all sublattices have the same ordering vector $\mathrm{X}_{\mathrm{1BZ}}$. $A_{\vec{q}}$ has maxima at opposite corners of four of the EBZ square surfaces, $(2\pi, 4\pi, 0)$, $(2\pi, 0, 4\pi)$, and subleading peaks with half maximum intensity at the four points $(0, \pm 2\pi, \pm 2\pi)$, consistent with the SLP ordering vector $\vec{Q}_{(0,1)} = \vec{Q}_{(2,3)} = (2\pi, 0, 0)$. The peak locations transform into each other by the D_{4h} subgroup of O_h. Thus, this phase is inversion symmetric, as opposed to the general SLP phase. This SLP-X phase extends both into the double-$\vec{q}$ and the general SLP regions at finite temperatures and will therefore generally cause two ordering transitions as the temperature is lowered from the disordered phase, first one into the SLP-X phase and then another into the double-$\vec{q}$ or general SLP phase at a lower temperature (see Fig. 6).

For $J_2 = J_{3b}$ at low temperatures, when biased into it, the NBT converges to an SLP-$(0, \pi, \pi)$ state where $A_{\vec{q}}$ also has D_{4h} symmetry. In this state the two spirals each reduce to a collinear configuration, one with ordering wave vectors $\vec{Q}_{(0,1)} = \pm(0, -\pi, \pi)$ and the other with $\vec{Q}_{(2,3)} = \pm(0, \pi, \pi)$. This state exists up to a finite temperature, but not all the way up to the disordered phase. We have not found the proper state at the intermediate temperatures, as we have not been able to get the NBT to converge in the shaded region in Fig. 6. Nevertheless, we have indicated phase boundaries around the SLP-$(0, \pi, \pi)$ phase as it necessarily must be separated by phase transitions from the inversion symmetry-breaking SLP phase surrounding it.

For sufficiently strong AF J_2, the SLP phase gives way to a single-$\vec{q}$ state with an ordering wave vector along the $\Gamma\mathrm{X}_{\mathrm{1BZ}}$ line. In this phase all sublattices order at the same wave vector, and the tetrahedra conditions are no longer satisfied. The phase boundary between the SLP phase and the $\Gamma\mathrm{X}_{\mathrm{1BZ}}$ phase is estimated to lie between $J_2 = 0.366$ and $J_2 = 0.374$ from our NBT calculations. The vertical line at $J_2 = 0.372$ is chosen from where the minimum of $J_{\vec{q}}$ changes character.

In Fig. 7 we map out the low-temperature phase diagram in the J_{3b}-J_2 coupling space using the NBT. It is seen that the SLP phase exists in a large region.

On the AF J_2 side, the SLP phase ceases to exist when it becomes energetically favorable to violate the tetrahedra conditions. For small and intermediate values of J_{3b} we find the single-$\vec{q}$ $\Gamma\mathrm{X}_{\mathrm{1BZ}}$ phase. For large J_{3b} the SLP phase is stable up to $J_2 = 1$, which is the limit set by the mapping from J_1-J_2 to $\tilde{J}_1$-$\tilde{J}_{3a}$.

On the FM J_2 side, the SLP phase borders the double-$\vec{q}$ phase where *each* sublattice has two ordering vectors. The

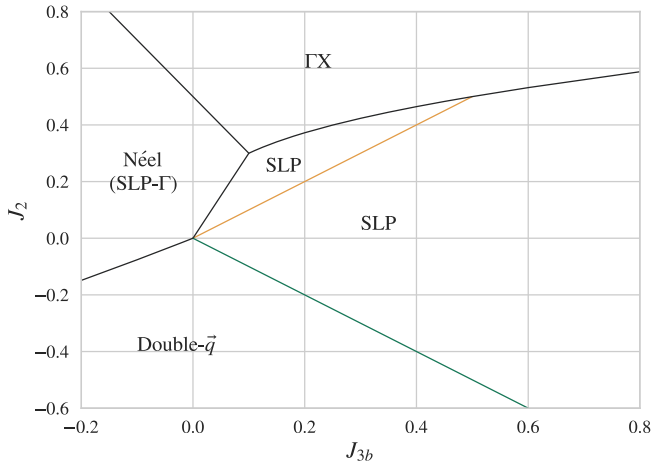

FIG. 7. Low-temperature phase diagram in the J_{3b}-J_2 coupling space, $J_{3a} = 0$. The inversion symmetric SLP-X and SLP-$(0, \pi, \pi)$ states are realized at $J_2 = -J_{3b}$ (green line) and $J_2 = J_{3b}$ (yellow line), respectively. For large AFM J_{3b}, the SLP state is stable for $-J_{3b} \leqslant J_2 < 1$.

two ordering vectors are $(2\pi, l, l)$ and $(2\pi, l, -l)$, where l increases from 0 (X_{1BZ}) to $\pi/2$ (U_{1BZ}) as J_{3b} decreases from $-J_2$. It reaches $\pi/2$ for J_{3b} equal to a small positive J_2-dependent value. For J_{3b} less than this, the two ordering vectors shift to $(0, k, k)$ and $(0, -k, k)$ with k decreasing slowly from $3\pi/2$ (K_{1BZ}) as J_{3b} decreases further. Spins in such double-$\vec{q}$ spirals will only obey the length constraint when the number of spin components $N_s > 3$. The NBT is derived from the large-N_s limit without vertex corrections and is extrapolated down to $N_s = 3$. We believe that the double-$\vec{q}$ state produced by NBT is a remnant of the large-N_s limit and that the extrapolation down to $N_s = 3$ does not take the length constraint sufficiently into account.

We have also performed a similar stability analysis in the J_{3b}-J_{3a} coupling space with J_2=0. There, for AFM J_{3b}, the SLP state is stable in an even wider region, whenever $J_{3a} \leqslant J_{3b}$.

To get information about the relative orientation of the spiral plane vectors $\vec{u}_{(i,j)}$ and $\vec{v}_{(i,j)}$ of the two SLP spirals, we have performed a spin wave calculation to compute the entropy. We find that entropy favors the SLP state to be coplanar for our model, Eq. (1), with the two SLP spirals sharing spiral plane vectors. Consequently, entropy favors collinear states in the special cases of SLP-Γ and SLP-X.

V. DISCUSSION

We have shown how the classical AFM Heisenberg model on the pyrochlore lattice with small further-neighbor couplings orders with coplanar SLP. In SLP, pairs of sublattices form antiparallel spirals. The ordering wave vectors are in general different for the two sublattice pairs and are found to be the wave vectors that minimize the total $\tilde{J}_{3a}$-J_{3b} energy of the paired fcc sublattices subject to the tetrahedra conditions.

For the pure J_1-J_{3b} model, we find a 120° SLP state. This state simultaneously satisfies both AFM J_1 and AFM J_{3b} and is thus realized for all $J_{3b} > 0$. It is separated from the disordered phase by a first-order phase transition with a T_c and latent heat that goes to zero as $J_{3b} \to 0$ (Fig. 5). This is consistent with the AFM nearest-neighbor model not ordering [1–4]. Note that the critical temperatures are likely to be overestimated as the NBT excludes vertex corrections [16].

The SLP state generally breaks inversion symmetry, except when four times the ordering wave vectors are reciprocal lattice vectors. We note that recent numerical results indicate that quantum fluctuations of the purely AF spin-1/2 and spin-1 models also induce inversion symmetry breaking [22–24].

As special cases of the SLP state, where all sublattices order at the same wave vector, we find SLP-Γ (Néel) and SLP-X for our model. SLP-Γ (Néel) has previously been identified as the ground state for the J_1-J_2 model with small AFM J_2 [7,21,25]. SLP-X is realized along the line $\tilde{J}_{3a} = J_{3b} > 0$ (and close to this line at intermediate temperatures) and should be the symmetry-broken state for the J_1-J_3 model in Ref. [12]. An *ab initio* study of the breathing pyrochlore material $LiGaCr_4O_8$ finds $\tilde{J}_{3a} = J_{3b} > 0$ and SLP-X as the corresponding low-temperature state [26]. They also find SLP-X to be stabilized at intermediate temperatures for $LiInCr_4O_8$, where $\tilde{J}_{3a} \approx 1.8 J_{3b} > 0$, which could be explained by the finite-temperature extension of the SLP-X phase due to its collinearity.

The J_2 and AFM J_{3a} bonds favor states which do not satisfy the tetrahedra conditions. Nevertheless, we find that the SLP state dominates a large portion of the exchange coupling space, particularly in the region $J_1 > J_{3b} > \tilde{J}_{3a}$ for AFM J_1 and J_{3b}.

This region might be relevant for the $Gd_2B_2O_7$ class of materials (B is a nonmagnetic cation) [9]. These are believed to be described as classical pyrochlore Heisenberg AFs with further-neighbor and dipole-dipole interactions [27–29]. While we have not considered the dipole-dipole interaction, we note that a recent experiment on $Gd_2Ti_2O_7$ suggests a partially ordered state with two ordering vectors at different L_{1BZ} points [30]. For SLP states such L peaks are most likely to occur at intermediate temperatures near the line $J_2 = J_{3b} > 0$ where there are line minima in-between the L_{1BZ} points.

The pyrochlore spinel materials are expected to have J_{3a} at the same order of magnitude as J_{3b} [10,11]. As we find the SLP phase to be stable for $J_{3a} \leqslant J_{3b}$ for AF J_{3b}, it could be of relevance also for this class of materials. Especially in the ferrites AFe_2O_4, the two types of third nearest-neighbor couplings have been suggested to be of comparable strength [11]. Inclusion of an AFM J_2 could also help to push the system towards the SLP phase.

We envision also the general SLP states to be realized on the breathing pyrochlore lattice when both the couplings J_1 and J_1' are sufficiently strong and antiferromagnetic, such that the tetrahedra conditions are satisfied. For further work it would be interesting to study the stability of the SLP state on the breathing pyrochlore lattice as well as its stability when adding dipolar interactions and/or anisotropy. We also note that the extension of the NBT to the pyrochlore lattice can be used to study other interesting problems such as possible symmetry breaking in the $J_2 = J_{3a}$ model [13].

ACKNOWLEDGMENTS

We would like to thank C. Castelnovo for pointing us in the direction of the J_1-J_{3b} model, and we thank J. Paaske and O. O. L. Solow for useful discussions about NBT. C.G. acknowledges funding from the Aker Scholarship. The computations were performed on resources provided by Sigma2, the National Infrastructure for High Performance Computing and Data Storage, in Norway.

[1] J. Villain, Insulating spin glasses, Z. Phys. B **33**, 31 (1979).

[2] J. N. Reimers, A. J. Berlinsky, and A.-C. Shi, Mean-field approach to magnetic ordering in highly frustrated pyrochlores, Phys. Rev. B **43**, 865 (1991).

[3] J. N. Reimers, Absence of long-range order in a three-dimensional geometrically frustrated antiferromagnet, Phys. Rev. B **45**, 7287 (1992).

[4] R. Moessner and J. T. Chalker, Properties of a Classical Spin Liquid: The Heisenberg Pyrochlore Antiferromagnet, Phys. Rev. Lett. **80**, 2929 (1998).

[5] T. Nakamura and D. Hirashima, Classical antiferromagnet on the pyrochlore lattice, J. Magn. Magn. Mater. **310**, 1297 (2007), Proceedings of the 17th International Conference on Magnetism.

[6] D. Tsuneishi, M. Ioki, and H. Kawamura, Novel ordering of the pyrochlore Heisenberg antiferromagnet with the ferromagnetic next-nearest-neighbour interaction, J. Phys.: Condens. Matter **19**, 145273 (2007).

[7] G.-W. Chern, R. Moessner, and O. Tchernyshyov, Partial order from disorder in a classical pyrochlore antiferromagnet, Phys. Rev. B **78**, 144418 (2008).

[8] T. Okubo, T. H. Nguyen, and H. Kawamura, Cubic and noncubic multiple-q states in the Heisenberg antiferromagnet on the pyrochlore lattice, Phys. Rev. B **84**, 144432 (2011).

[9] A. S. Wills, M. E. Zhitomirsky, B. Canals, J. P. Sanchez, P. Bonville, P. D. de Réotier, and A. Yaouanc, Magnetic ordering in $Gd_2Sn_2O_7$: the archetypal Heisenberg pyrochlore antiferromagnet, J. Phys.: Condens. Matter **18**, L37 (2006).

[10] A. N. Yaresko, Electronic band structure and exchange coupling constants in ACr_2X_4 spinels (A = Zn, Cd, and Hg; X = O, S, and Se), Phys. Rev. B **77**, 115106 (2008).

[11] C. Cheng, Long-range antiferromagnetic interactions in $ZnFe_2O_4$ and $CdFe_2O_4$: Density functional theory calculations, Phys. Rev. B **78**, 132403 (2008).

[12] P. H. Conlon and J. T. Chalker, Absent pinch points and emergent clusters: Further neighbor interactions in the pyrochlore Heisenberg antiferromagnet, Phys. Rev. B **81**, 224413 (2010).

[13] T. Mizoguchi, L. D. C. Jaubert, R. Moessner, and M. Udagawa, Magnetic clustering, half-moons, and shadow pinch points as signals of a proximate Coulomb phase in frustrated Heisenberg magnets, Phys. Rev. B **98**, 144446 (2018).

[14] S. E. Palmer and J. T. Chalker, Order induced by dipolar interactions in a geometrically frustrated antiferromagnet, Phys. Rev. B **62**, 488 (2000).

[15] M. Schecter, O. F. Syljuåsen, and J. Paaske, Nematic Bond Theory of Heisenberg Helimagnets, Phys. Rev. Lett. **119**, 157202 (2017).

[16] O. F. Syljuåsen, J. Paaske, and M. Schecter, Interplay between magnetic and vestigial nematic orders in the layered J_1-J_2 classical Heisenberg model, Phys. Rev. B **99**, 174404 (2019).

[17] C. Glittum and O. F. Syljuåsen, Arc-shaped structure factor in the $J_1-J_2-J_3$ classical Heisenberg model on the triangular lattice, Phys. Rev. B **104**, 184427 (2021).

[18] J. Liu, X.-P. Yao, and G. Chen, Stacking-induced magnetic frustration and spiral spin liquid, Phys. Rev. B **106**, L220410 (2022).

[19] We use the same labeling of points in the EBZ as in Ref. [25].

[20] The specific symmetry-breaking pattern depends on the random initial value of $\Sigma_{\vec{q}}$. In all cases Eq. (5) is obeyed.

[21] M. F. Lapa and C. L. Henley, Ground states of the classical antiferromagnet on the pyrochlore lattice, arXiv:1210.6810.

[22] I. Hagymási, R. Schäfer, R. Moessner, and D. J. Luitz, Possible Inversion Symmetry Breaking in the $S = 1/2$ Pyrochlore Heisenberg Magnet, Phys. Rev. Lett. **126**, 117204 (2021).

[23] N. Astrakhantsev, T. Westerhout, A. Tiwari, K. Choo, A. Chen, M. H. Fischer, G. Carleo, and T. Neupert, Broken-Symmetry Ground States of the Heisenberg Model on the Pyrochlore Lattice, Phys. Rev. X **11**, 041021 (2021).

[24] I. Hagymási, V. Noculak, and J. Reuther, Enhanced symmetry-breaking tendencies in the $S = 1$ pyrochlore antiferromagnet, Phys. Rev. B **106**, 235137 (2022).

[25] Y. Iqbal, T. Müller, P. Ghosh, M. J. P. Gingras, H. O. Jeschke, S. Rachel, J. Reuther, and R. Thomale, Quantum and Classical Phases of the Pyrochlore Heisenberg Model with Competing Interactions, Phys. Rev. X **9**, 011005 (2019).

[26] P. Ghosh, Y. Iqbal, T. Müller, R. T. Ponnaganti, R. Thomale, R. Narayanan, J. Reuther, M. J. P. Gingras, and H. O. Jeschke, Breathing chromium spinels: a showcase for a variety of pyrochlore Heisenberg Hamiltonians, npj Quantum Mater. **4**, 63 (2019).

[27] N. P. Raju, M. Dion, M. J. P. Gingras, T. E. Mason, and J. E. Greedan, Transition to long-range magnetic order in the highly frustrated insulating pyrochlore antiferromagnet $Gd_2Ti_2O_7$, Phys. Rev. B **59**, 14489 (1999).

[28] A. P. Ramirez, B. S. Shastry, A. Hayashi, J. J. Krajewski, D. A. Huse, and R. J. Cava, Multiple Field-Induced Phase Transitions in the Geometrically Frustrated Dipolar Magnet: $Gd_2Ti_2O_7$, Phys. Rev. Lett. **89**, 067202 (2002).

[29] P. G. Welch, J. A. M. Paddison, M. D. Le, J. S. Gardner, W.-T. Chen, A. R. Wildes, A. L. Goodwin, and J. R. Stewart, Magnetic structure and exchange interactions in the Heisenberg pyrochlore antiferromagnet $Gd_2Pt_2O_7$, Phys. Rev. B **105**, 094402 (2022).

[30] J. A. M. Paddison, G. Ehlers, A. B. Cairns, J. S. Gardner, O. A. Petrenko, N. P. Butch, D. D. Khalyavin, P. Manuel, H. E. Fischer, H. Zhou, A. L. Goodwin, and J. R. Stewart, Suppressed-moment 2-k order in the canonical frustrated antiferromagnet $Gd_2Ti_2O_7$, npj Quantum Mater. **6**, 99 (2021).